Available online at www.sciencedirect.com
SCIENCE DIRECT®
Journal of Magnetic Resonance 178 (2006) 25–32
JMR Journal of Magnetic Resonance
www.elsevier.com/locate/jmr

# Quantitative density profiling with pure phase encoding and a dedicated 1D gradient

K. Deka [a], M.B. MacMillan [a], A.V. Ouriadov [a], I.V. Mastikhin [a], J.J. Young [a], P.M. Glover [b], G.R. Ziegler [c], B.J. Balcom [a,*]

[a] MRI Centre, Department of Physics, University of New Brunswick, P.O. Box 4400, Fredericton, NB, Canada E3B 5A3
[b] Sir Peter Mansfield Magnetic Resonance Center, School of Physics and Astronomy, University of Nottingham, University Park, Nottingham, NG7 2RD, UK
[c] 116 Borland Lab, Department of Food Science, Penn State University, University Park, PA 16802, USA

Received 18 July 2005; revised 23 August 2005
Available online 26 September 2005

**Abstract**

A new centric scan imaging methodology for density profiling of materials with short transverse relaxation times is presented. This method is shown to be more robust than our previously reported centric scan pure phase encode methodologies. The method is particularly well suited to density imaging of low gyro-magnetic ratio non-proton nuclei through the use of a novel dedicated one-dimensional magnetic field gradient coil. The design and construction of this multi-layer, water cooled, gradient coil is presented. Although of large diameter (7.62 cm) to maximize sample cross section, the gradient coil has an efficiency of several times that offered by conventional designs (6 mT/m/A). The application of these ideas is illustrated with high resolution density-weighted proton ($^1$H) images of hazelnut oil penetration into chocolate, and lithium ion ($^7$Li) penetration into cement paste. The methods described in this paper provide a straightforward and reliable means for imaging a class of samples that, until now, have been very difficult to image.


*Keywords:* Centric scan; Relaxation time; Non-proton; Gradient coil; SPRITE; Density-weighted

## 1. Introduction

Most MRI methods inherently have relaxation time contrast. In many instances this is seen as a positive feature of MRI. However, true quantitative imaging in many realistic materials imaging problems requires that density weighting be recovered. In an ideal scenario, this simply involves a pixel-by-pixel re-scaling based upon known relaxation times, but in practice it is rarely this straightforward.

Short signal lifetimes ($T_2^* < 10$ μs) are common in solid materials, and while a number of MRI profiling methods for such systems currently exist, all are plagued by significant disadvantages. With frequency encode methods, attenuation of the echo train is due to both $T_1$ and $T_2$ processes as well as diffusion, making quantitative interpretation of the signal intensity difficult. Hurlimann [1] has reported that the relaxation decay of the signal amplitude is non-exponential, even if the sample has a single $T_1$, $T_2$, and diffusion coefficient. A CPMG or Ostroff-Waugh approach may yield a reliable estimate of the transverse relaxation and diffusion effects for special cases where $T_1 >> T_2$, but this is not true if, as often happens, $T_1$ and $T_2$ are multi-exponential.

The STRAFI [2–5] technique offers high resolution but the signal suffers heavily from relaxation time weighting, making it difficult to quantify true proton density. STRAFI employs the strong, time invariant magnetic field gradient in the periphery of permanent or superconducting magnets. The fixed gradient, while necessary for high resolution imaging of short $T_2$ samples, does give rise to several significant disadvantages, such as off-resonance RF pulse excitation, with the result that echo trains in STRAFI often do not behave in a simple exponential manner.

* Corresponding author. Fax: +1 506 453 4581.
*E-mail address:* bjb@unb.ca (B.J. Balcom).

1090-7807/$ - see front matter © 2005 Elsevier Inc. All rights reserved.
doi:10.1016/j.jmr.2005.08.009

Kopinga and Pel [6] outline a spin echo profiling technique which uses large static gradients and achieves submillimeter resolution. Slice selection is accomplished either through adjustment of the r.f. carrier frequency or physical translation of the sample through the sensitive region of their r.f. coil.

An advantageous feature of this method is it's applicability to samples with dimensions larger than the field of view (FOV). However, since spin-echo methods can not be reliably applied to samples where the relaxation times are shorter than the minimum echo time [7], the necessity of generating an echo means that it may be difficult or impossible to observe the shortest lived signal components with this method. Also, in cases where multiple relaxation times are present, quantification of the individual spin groups will be problematic.

Quantitative 3D imaging in general imposes a significant time penalty. Many physical problems (e.g., transport within materials), however, can be reduced to a 1D geometry, and therefore 1D profiling is often the most efficient approach to MRI analysis of materials. Time resolution of dynamic physical processes can most easily be achieved using 1D MRI scans because of the dramatic speed improvements compared to 2D or 3D imaging. 1D profiles are also usually simpler to understand and analyze compared to higher dimensionality imaging. This paper describes the development and applications of a density imaging technique based on a 1D centric scan SPRITE (single point imaging with $T_1$ enhancement) [8] methodology using a dedicated magnetic field gradient system.

The SPRITE technique, as a pure phase encode method, does not require echo formation, or sample translation, and employs only brief duration, broadband, RF pulses. The earliest version of SPRITE [8] was susceptible to magnetization saturation due to the order in which its repetitive series of r.f. pulses traversed $k$-space. With centrically scanned SPRITE sequences, the acquisition starts from the center of $k$-space before any magnetization saturation has occurred, thus yielding an image free of $T_1$ weighting.

The original 1D centric scan SPRITE technique [9] suffered from image artifacts whenever background gradients were present. In the method presented here, we use a centric scan approach which addresses the distortions arising from background gradients.

In this work, we have also considered the problem of quantitative density imaging of low $\gamma$ nuclei. We have designed and built a high-strength magnetic field gradient system to compensate for the smaller range of $k$-space available to low $\gamma$ nuclei. The new gradient system is a dedicated multi-layered gradient coil set [10,11] with a relatively large (7.62 cm) internal diameter. We have used the new 1D centric SPRITE technique in tandem with the dedicated gradient coil set to undertake dynamic profiling measurements of $^1$H and $^7$Li species. Back extrapolation of the signal decay curve is used to extract nuclear spin density weighted images of the $^1$H and $^7$Li samples.

## 2. Theory

### 2.1. 1D centric scan SPRITE technique

A centric scan SPRITE acquisition [9] samples the central point of $k$-space first, such that no $T_1$ weighting is introduced at the $k$-space origin. The local image intensity at any point in the image is thus given by

$$S = \rho \exp\left(-\frac{t_p}{T_2^*}\right) \sin\alpha, \tag{1}$$

where $\rho$ is the spin density, $\alpha$ the RF flip angle and $t_p$ the phase encode time. The opportunity offered by Eq. (1) is clear. For centric scan imaging, when $t_p \ll T_2^*$, the resulting image is directly proportional to the local spin density, given that $\sin\alpha$ is a simple geometric factor which is ideally constant over the field of view. This is in contrast to the original SPRITE technique [8] which featured significant $T_1$ contrast in the signal equation.

Blurring due to the decay of the longitudinal magnetization with repetitive RF pulses [9] limits the choice of flip angle, $\alpha$. The centric scan technique nevertheless yields more signal and, compared to the original implementation, minimizes the measurement time.

In our original half-$k$-space SPRITE paper [9], half of $k$-space was sampled with the SPRITE sequence, from 0 to $+k_z$. The missing half was reconstructed using the inherent symmetry of $k$-space. Ideally, the image is reconstructed by finding $F(-k_z)$ via the symmetry of the complex conjugate [12]

$$F(-k_z) = F^*(k_z). \tag{2}$$

However, this is possible only when $\rho(z)$ is a real function. In practice, due to inhomogeneities in the $B_0$ field, $\rho(z)$ is effectively complex. If we invoke conjugate symmetry with this complex object then the Fourier reconstruction method will not yield an accurate representation of $\rho(z)$.

The double half-$k$-space (DHK) technique illustrated in Fig. 1 has the advantages of centric scanning yet provides immunity to background gradients. In the DHK methodology, $k$-space is scanned sequentially from 0 to $+k_z$ and,

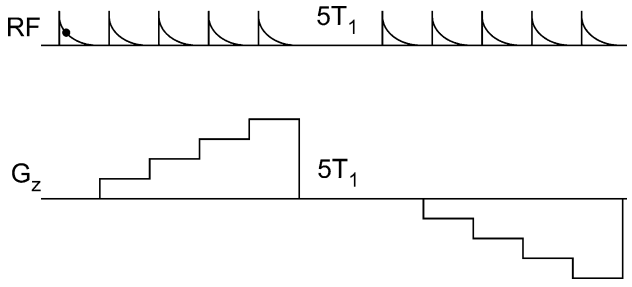


Fig. 1. The one-dimensional DHK-SPRITE sequence. The magnetic field gradient ($G_z$) is ramped linearly in steps to $+G_z$ in the 1st half of the measurement and to $-G_z$ in the 2nd half. A single data point is acquired at each gradient step at a time $t_p$ after the application of a radio frequency (RF) pulse of flip angle $\alpha$. A time delay of $5T_1$ separates the two halves of the acquisition.

after a delay equal to $5T_1$, again from 0 to $-k_z$. The common 0 points are averaged and the data arranged in a single linear array prior to FFT. The DHK method precludes the formation of unwanted echoes through the passive spoiling induced by incrementing the phase encode gradients.

### 2.2. Multi-layer gradient coil

With pure phase encode techniques, the FOV is related to the encoding time, $t_p$, via

$$\mathrm{FOV} = \frac{1}{\Delta k} = \frac{1}{\frac{1}{2\pi}\gamma \Delta G t_p}. \tag{3}$$

If we wish a narrow FOV (~1–2 cm) with a $t_p$ on the order of tens of μs then, from Eq. (3), $\Delta G$, and therefore $G_{max}$, must be large, on the order of thousands of $\mathrm{mTm}^{-1}$. Additionally, to image nuclei other than proton, where $\gamma$ will be reduced from the proton value, quite substantially so in some cases, one must compensate through increased $t_p$ or $\Delta G$, if the FOV is to remain the same.

Gradient coil design [10,11] is usually a tradeoff between the gradient strength per unit current (usually known as the gradient coil efficiency), $\eta$, inductance, $L$, resistance, $R$, and the size of the region within which the field variation is linear with position. Increased efficiency usually leads to decreased linearity. Higher inductance, which in turn implies longer gradient rise times, $\tau$, and higher resistance, results in greater power dissipation in the coil. The maximum amplifier current, $I_a$, is limited by the amplifier, and $nI_a$, which determines the magnetic field gradient, is limited by the number of turns, $n$, in the gradient coil. As $n$ is increased the inductance becomes large and makes it impossible to achieve an acceptable gradient rise time, $\tau$, for traditional echo based MRI methods [11], i.e.

$$\tau \approx \frac{LI_a}{V_a}, \tag{4}$$

where $V_a$ is the amplifier voltage.

An increased rise time is not critical to SPRITE measurements, however, as we apply the primary phase encode gradient in linear steps with a repetition time of typically between 1 and 4 ms. The repetition time is thus the important parameter related to the rise time $\tau$ and it is substantially longer than the time constants associated with echo formation in conventional imaging.

To accommodate $n$ turns of wire in a cylindrical coil with a fixed length and radius $a$, the wire radius must decrease as $n$ increases [11]. Thus, the coil resistance increases rapidly with $n$ due to the decrease in the wire cross-sectional area as well as the increase in length of the wire. Therefore, in traditional designs

$$R \propto \frac{n^3}{a}. \tag{5}$$

For this case, a efficiency scales with resistance [10] as

$$\eta \propto R^{1/3}. \tag{6}$$

The rapid increase in resistance with the number of turns imposes a limit on the attainable gradient strength through the practical limitations on the available amplifier voltage. This problem can be overcome by adopting a multilayer coil design in which the coil radius is increased incrementally in successive layers. In this design with the inner and outer radii of the layers fixed, the efficiency scales as [11]

$$\eta \propto R^{1/2}. \tag{7}$$

The multilayer coil approach [11] makes it possible to achieve much higher gradient strengths, while maintaining reasonable coil resistance and power dissipation.

### 2.3. Density profiling

To extract true nuclear density weighted images from short-lived NMR signals, one needs to encode for a very short time. Implementation of a high strength magnetic field gradient, which therefore permits large gradient increments $\Delta G$, enables us to use an encoding time as short as tens of μs while still retaining an acceptable FOV (Eq. (3)).

The intensity of the reconstructed image is weighted by $T_2^*$ and the encoding time $t_p$ according to Eq. (1). If this weighting is significant, then true spin density can be recovered from a series of images with variable $t_p$, but constant FOV. As a pure phase encode technique, SPRITE is immune to distortions from $B_0$ inhomogeneities, magnetic susceptibility variations, and chemical shift. A fit of pixel intensity to $t_p$ will yield a $T_2^*$ map and, by back-extrapolation, a pure density image.

### 2.4. Zero-filling to further reduce encoding time ($t_p$)

From Eq. (1), if $t_p << T_2^*$, then $S \propto \rho$. There is an imperative, therefore, in reducing $t_p$ without sacrificing the FOV. Our approach, as outlined earlier, is to increase $\Delta G$. We also invoke a simple zero filling strategy which permits us to reduce $t_p$ by a further factor of 2. From Eq. (3) it is clear that if $t_p$ is halved, $\Delta G$ must be doubled to maintain the same FOV. Since the maximum possible gradient value is fixed, this decreases the number of sampled points, hence resolution, by a factor of 2. We are able to maintain full $k$-space sampling if we simply zero fill the remaining points, thereby regaining the original nominal resolution.

Zero-filling improves the digital resolution of an image by interpolating between sampled data points [13]. Although it is a convenient method for extending the range of data points to improve resolution, this is not our primary goal. We zero-fill (×2) to reduce $t_p$ (×2) and remove or reduce $T_2^*$ weighting from our images. The interpolation which results is not a problem for profiles of the type anticipated for this method, since we expect relatively smooth experimental profiles.

### 2.5. Non-proton imaging

Imaging of species other than proton is often a challenge. This is due in part to the lower gyromagnetic ratio ($\gamma$) of these nuclei. For example $\gamma$ for $^{7}$Li, $^{23}$Na, and $^{35}$Cl is 40, 30, and 10%, respectively, of that for $^{1}$H [14]. Since the inherent sensitivity varies as $\gamma^3$, the image quality will naturally be reduced. Additionally, to acquire an image with the same FOV as $^{1}$H requires either longer encoding times or higher gradient strengths. Since our interest in non-proton species is principally associated with porous media where $T_2^*$ is short, we must rely on the latter.

Our approach to this type of imaging employs a high strength, one dimensional gradient coil set. We have maximized the gradient coil internal diameter, allowing for larger r.f. probes and samples. Since the quantity of material per unit length varies with $r^2$, and NMR sensitivity as $1/r$ (assuming constant length), doubling the sample diameter results in a factor of 2 gain in SNR.

## 3. Results and discussion

### 3.1. High strength magnetic field gradient set

The custom built 1D $Z$-gradient set, Fig. 2, is a conventional Maxwell pair wound on a cylindrical nylon tube of 7.62 cm inner diameter. Four layers of copper wire, 11 AWG HAPT 200 C,Wiretronic Inc.(Pinegrove, CA), with 24 turns, including a correction coil [10], were employed. Extensive water cooling in the gradient set enabled us to maintain the temperature under 17 °C with a maximum sustained current of 140 A.

The new gradient set has an efficiency of 15 $\mathrm{mTm^{-1}A^{-1}}$, a resistance of 0.36 Ω, and an inductance of 1.61 mH. The gradient magnetic field, measured experimentally, deviates from linearity by less than 5% within a central cylindrical region 8 cm in length and 4 cm in diameter. These parameters are in close agreement with predictions from simulation. The gradient set can produce a maximum gradient of 3000 $\mathrm{mTm^{-1}}$ with the Techron 8710 power supply. The internal diameter is 7.62 cm, permitting a 4.3 cm diameter sample with a family of quadrature birdcage coils for $^{1}$H and other nuclei. This 1D gradient set has been used for all imaging discussed here.

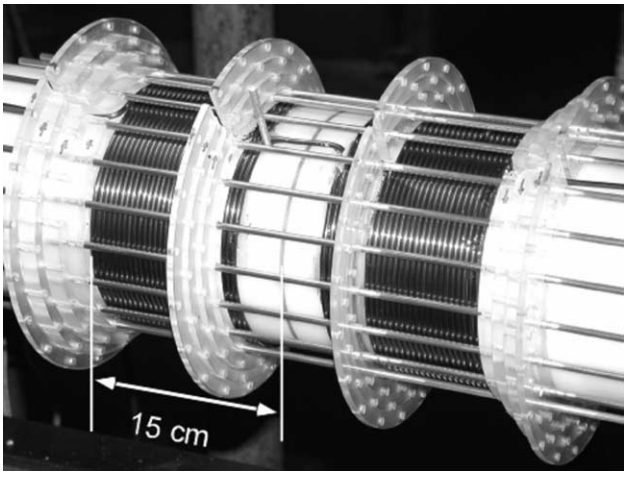


Fig. 2. A photograph of the custom built gradient set, showing the 1st wire layer and placement of the first layer of cooling tubes. The coil, with 24 turns, including three turns for a correction coil, on each side of the gradient, was 30 cm in length. The internal diameter of the gradient is 7.62 cm, with an efficiency $\eta = 15\ \mathrm{mTm^{-1}\ A^{-1}}$.

### 3.2. 1D DHK SPRITE technique

The reliability of this new technique is demonstrated by imaging a plastic (delrin) phantom with a geometry illustrated in Fig. 3A. For this $^{1}$H measurement, we added a 15 $\mathrm{mTm^{-1}}$ background gradient by supplying a constant current to the $Z$ shim. The experimental DHK image yields a geometrically correct phantom image, Fig. 3B. By contrast, the same phantom reconstructed from a data set with one half of $k$-space determined by conjugation of the other half yields a highly distorted, low quality image, Fig. 3C. The DHK SPRITE technique has a demonstratively better signal to noise ratio (SNR) compared to the single half-$k$ acquisition technique, even when considering that DHK collects twice the number of data points.

### 3.3. $^{1}$H density profiling

Oil migration is responsible for the limited shelf life of composite confectionery products, for example those containing centers, coated biscuits, and nut inclusions [15]. Quality defects arising from oil migration include softening of the coating, hardening of the filling, deterioration in sensory quality and a greater tendency to fat bloom formation at the surface of the product [16,17]. For this reason, oil migration in chocolate confectioneries has been extensively studied.

Despite the attention, mechanistic studies of oil migration are lacking in the literature. This is due in part to the lack of a straightforward, quantitative, non-destructive investigative technique. However, a mechanistic understanding is essential if one is to develop strategies to hinder fat bloom in chocolate confectionery.

Dark chocolate is a mixture of cocoa liquor, cocoa butter, and sugar containing solid and liquid lipid at room temperature. A monotectic mixture with cocoa butter will be formed due to migration of foreign lipid from an oil-containing filling or inclusion. Oil migration involves the coupling of two complex phenomenon, molecular diffusion and phase behavior [15].

In previous NMR work by other groups [16,17], the signal was acquired several milliseconds after RF excitation, so that the signal detected arose solely from the liquid fat, since the signal from solid fat decays too rapidly. However, an acquisition time of several milliseconds does not provide true quantitative information about liquid lipid in the sample. Quantitative spatially resolved

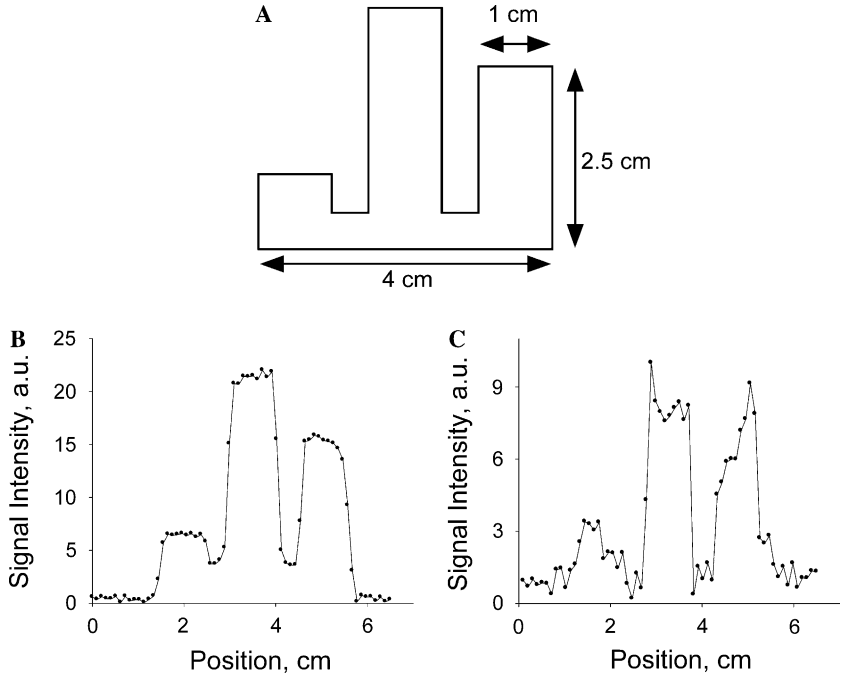


Fig. 3. (A) A schematic diagram of the delrin phantom with three distinct lobes of 1, 3.5, and 2.5 cm height. Each lobe was 1 cm wide with a 0.5 cm gap between each lobe. (B) A 1D $^1$H DHK SPRITE image of the plastic phantom illustrated in (A). The image is geometrically correct, despite the presence of a 15 mTm$^{-1}$ background gradient. (C) A 1D $^1$H single half-$k$ SPRITE image of the delrin phantom with a 15 mTm$^{-1}$ background gradient. One half of the $k$-space data was conjugated to form a complete data set prior to FFT. The image is significantly degraded compared to (B).

measurements of liquid fat therefore require the inclusion of a calibrated reference [16].

In this work, we have taken advantage of the centric scan SPRITE technique, coupled with a high strength magnetic field gradient coil set, to acquire images with a short encoding time. This enabled us to quantitatively observe the liquid lipid present in the sample.

The FID of our chocolate sample prior to exposure to the oil is a superposition of two line shapes arising from the solid and liquid phases. The short component is a Gaussian, which decayed to 5% in 13 μs, the long one an exponential with a $T_2^*$ of 800 μs.

A chocolate sample was exposed to hazelnut oil and imaged as a function of exposure time using $t_p = 100$ μs (see Fig. 4). Since the liquid lipid $T_2^* \gg t_p$, these are effectively density weighted profiles which give a map of oil concentration as a function of time. The observed signal intensity increases with exposure, as the intrusion of hazelnut oil results in an increase in the liquid lipid component relative to the solid component.

For $^1$H density profiling we acquired several 1D DHK profiles of chocolate (without exposure to hazelnut oil) at different $t_p$'s, while maintaining a constant FOV (see Fig. 5). The shortest $t_p$ was 100 μs, chosen to avoid any contribution from the solid component. Signal decay curves were extracted for each pixel in the image (see Fig. 6A). Back extrapolating the signal decay curves removes $T_2^*$ weighting [18], yielding spatially resolved density images of liquid lipid in the chocolate (see Fig. 6B).

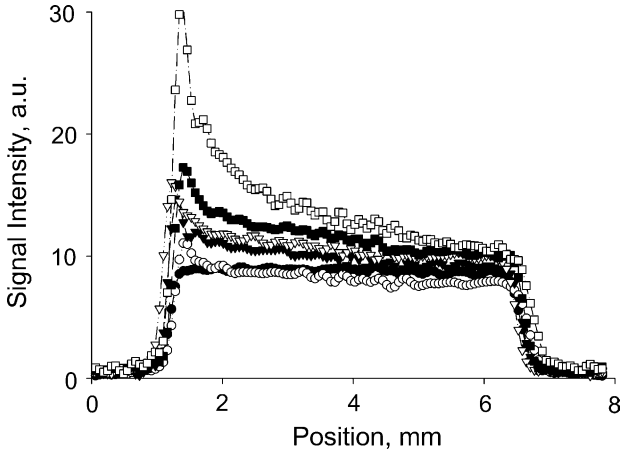


Fig. 4. 1D $^1$H DHK SPRITE images of Hazelnut oil absorption into the chocolate sample. The symbols ●, ○, ▼, ▽, ■, □ correspond to 0, 2, 4, 6, 8, and 18 h of exposure to the oil. Oil penetration is from the left side of the image. An encoding time of 100 μs was used. The acquisition time for each measurement was 140 s.

For an absolute quantification of spin density, we would include a reference material whose proton concentration was known. Since our approach removes relaxation time weighting, this would provide an absolute density reference. In a study of similar chocolate and oil systems using spin-echo measurements, Guiheneuf et al. [16] employed a hazelnut oil reference for calibration. This requires, however, that the reference has the same $T_2$ as the sample. This is unlikely to be true under all conditions, particularly so when multiple relaxation times are present.

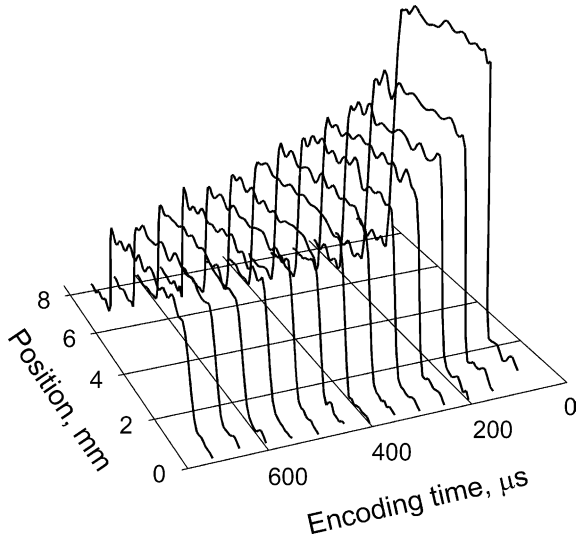


Fig. 5. $T_2^*$ weighted 1D DHK SPRITE images of the uniform chocolate sample without oil exposure. Thirteen profiles are plotted in 50 μs intervals in $t_p$, starting from 100 μs. These images represent the liquid lipid present in the chocolate sample.

A more complete oil-invasion study is currently underway, and will be reported in the near future.

### 3.4. Dynamic density weighted imaging of lithium ions

Lithium is a relatively uncommon nucleus for MRI [19], but one which is of increasing importance in cement based materials. It is highly desirable to be able to directly measure the distribution of lithium in such applications. Lithium is used in concrete to suppress alkali-silica reactions (ASR) [20–22], which can damage concrete structures by inducing cracking.

The lithium MRI relaxation times in cement based materials are relatively short by traditional MRI standards, with a $T_1$ typically of several ms, and a $T_2^*$ of approximately 100 μs. The only measurable signal arises from lithium ions within the pore solution to be measured. Lithium in a crystalline form, or physically or chemically bound, is not observed. While this may appear as a limitation, with respect to alkali-silica reactivity it is the lithium available in the pore solution that is important.

1D DHK-SPRITE profiles with a nominal resolution of 1.56 mm were acquired for two samples as a function of adsorption time, as shown in Fig. 7. In this case, a reference of $LiNO_3$ in solution is used to compensate for long term variations in the sensitivity of the instrument. For these measurements no correction was necessary. As expected, the penetration depth increased with contact time. After 22 h, lithium had penetrated approximately 35 mm. In addition, the signal intensity at a given point within the penetration region, and therefore the local lithium concentration, increased with time.

As in the previous case, density weighted images on a homogeneously Li loaded sample were acquired using multiple 1D profiles, all with a constant FOV (see Fig. 8). Back

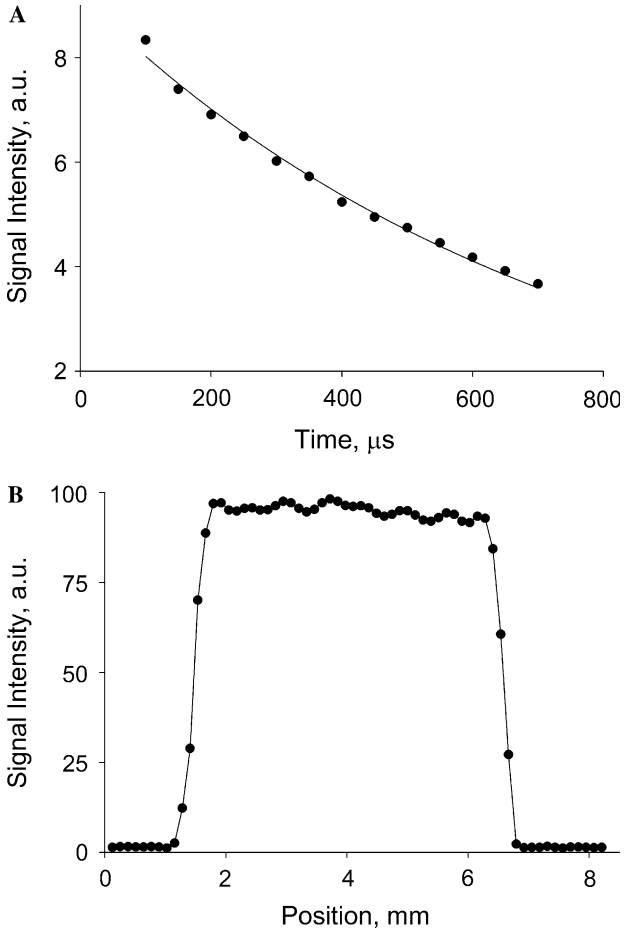


Fig. 6. (A) The image intensity from an arbitrarily chosen pixel from the chocolate sample, extracted from each 1D $T_2^*$ weighted $^1H$ image. The image intensity is plotted against the corresponding $t_p$ value to obtain a $T_2^*$ decay curve. The line of best fit to a single exponential decay function yields a $T_2^*$ of 750 μs, which agrees well with the bulk value of 800 μs. (B) A 1D $^1H$ nuclear spin density weighted image of liquid lipid in the chocolate sample, acquired via back-extrapolation of the signal decay curve for each pixel in the image.

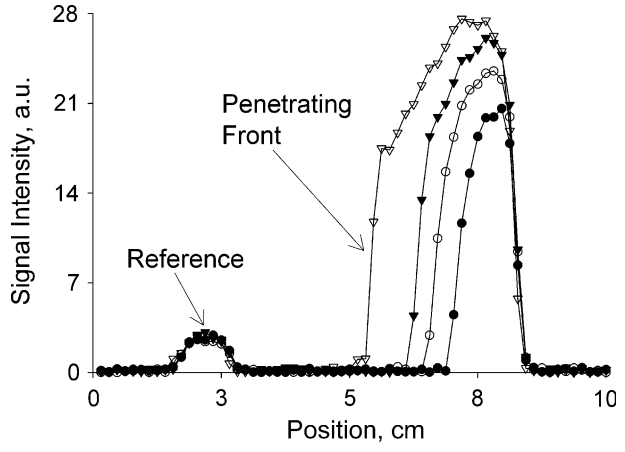


Fig. 7. 1D $^7Li$ DHK-SPRITE images of Lithium absorption into a cement paste mortar. A reference sample is included as a check on the long term instrument stability. The images represent the lithium distribution after 3 (●), 6 (○), 9 (▼), and 22 (▽) hours of exposure.

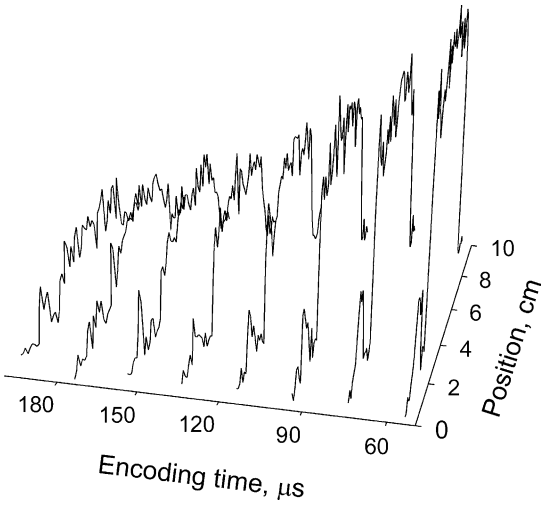


Fig. 8. $T_2^*$ weighted 1D $^7$Li DHK SPRITE images of $^7$Li containing type 10 Portland cement paste and a reference sample. The sample was prepared with a uniform lithium distribution. The water to cement ratio of the cement paste was 0.5. Eight 1D profiles with $t_p$s ranging from 54 to 194 μs, in 20 μs increments, are plotted. While paramagnetic impurities in type 10 cement typically result in a very short $^1$H $T_2^*$, this is not a problem with lithium.

extrapolation of the signal decay curve (Fig. 9A) removes the $T_2^*$ weighting (Fig. 9B). The measured $T_2^*$ was consistent at 100 μs, which agreed well with measured bulk value of 110 μs.

## 4. Conclusion

The robust nature of the DHK technique has been proven in the current work, as has its utility for imaging short $T_2^*$ materials. A dedicated high strength magnetic field gradient coil set permits nuclear spin density weighted imaging of nuclei with low gyromagnetic ratio.

NMR, when coupled with imaging (MRI), can give information about the structure and spatial distribution of lipid in chocolate materials. As NMR/MRI is a non destructive method, time lapse studies can be carried out on a single sample. Based on the equipment and measurement techniques described here, we will shortly be reporting studies of the solid lipid present in chocolate.

We have implemented the new methodology for imaging $^7$Li in a cement paste. MRI has the potential to play an important role in concrete technology. While this method has been developed for laboratory studies, measurements could be made on cores extracted from existing concrete structures. While traditional methods such as pore solution extraction provide valuable information, MRI can provide additional information in that lithium MRI profiles yield a spatial concentration of lithium, with sub-millimeter resolution, in less than one hour. The additional information permits diffusion coefficients and penetration rates to be accurately determined.

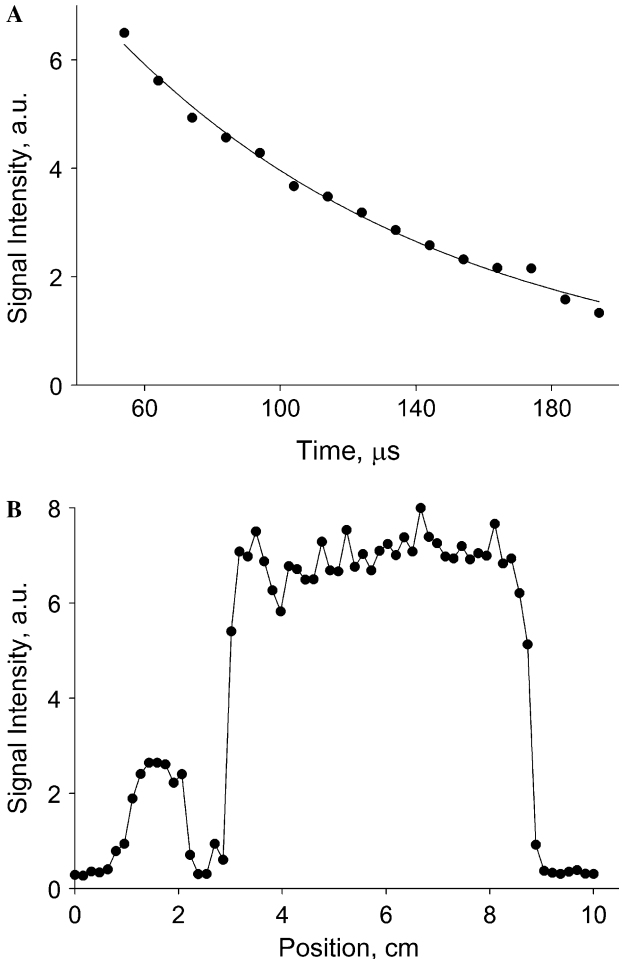


Fig. 9. (A) The signal intensity at each pixel, extracted from multiple 1D $T_2^*$ weighted images. The line of best fit to a single exponential decay function yields a $T_2^*$ of 100 μs, in agreement with the bulk value of 110 μs. (B) 1D nuclear density weighted image of lithium containing cement paste and a reference sample acquired from pixel-by pixel back-extrapolation of the signal decay curves.

## 5. Experimental

All imaging experiments employed a Nalorac (Martinex, CA) 2.4 T 32 cm i.d. horizontal bore superconducting magnet. The console was a Tecmag (Houston, TX) Apollo. All experiments were performed at ambient temperature, approximately 12 °C.

The custom built 1D gradient coil set 7.62 cm (i.d), was driven by a Techron (Elkhart, IN) 8710 amplifier. An eight-rung birdcage $^1$H probe (Morris Instrument, Ottawa), driven in quadrature by a 2 kW AMT (Brea,CA)3445 RF amplifier, was employed for phantom imaging. In all experiments the FID was used to measure the bulk $T_2^*$. Inversion recovery measurements were made to measure the bulk $T_1$.

The relaxation times of the delrin phantom were: $T_1 = 970$ ms and $T_2^* = 250$ μs. The phantom imaging parameters were: $t_p = 30$ μs, FOV = 6.5 cm, TR = 2 ms, $a = 5°$, number of pixels = 64, $G_{max} = 390$ mTm$^{-1}$, 8 averages were acquired with an acquisition time of 49 s.

For $^1$H imaging a piece of dark chocolate (Lindt Excellence 70%, France) was cut into a 2 cm diameter disc with a thickness of 0.5 cm. 1D DHK SPRITE images were acquired with $t_p$ varying from 100 to 700 μs in 50 μs increments. The bulk $T_1$ of the chocolate sample was 183 ms. The FID was a superposition of a Gaussian, which decayed to 5% in 13 μs, and an exponential with a $T_2^*$ of 800 μs. A total of 32 data points were acquired using the 1D DHK SPRITE technique with $\alpha = 10°$ and $G_{max} = 460\ mTm^{-1}$. The dataset was zero filled to 64 *k*-space points. The FOV for these measurements was 0.81 cm.

Oil migration measurements in chocolate (Lindt excellence 70%, France) were carried out by acquiring 32 *k*-space data points, subsequently zero filled to 64. Implementation of zero-filling enabled us to encode the MR signal at 100 μs using $G_{max} = 480\ mTm^{-1}$, TR = 2 ms, FOV = 0.78 cm, $\alpha = 10°$, 64 averages and a 140 s acquisition time. A thick piece of tissue paper was soaked in hazelnut oil and a chocolate disc (2 cm diameter) was placed on the tissue paper in a petri dish. The oil treatment was undertaken at 23 °C and 50% RH. The chocolate was removed from the tissue paper for imaging.

Lithium imaging was undertaken using a cement paste containing Lithium ($^7$Li) and a reference sample of $LiNO_3$ in solution. Imaging employed a custom built eight-rung lithium birdcage coil driven in single channel mode by a 2 kW AMT (Brea, CA) 3445 RF amplifier. Bulk relaxation times for this sample were: $T_1 = 3$ ms and $T_2^* = 110$ μs. 1D DHK SPRITE images were acquired at different encoding times ranging from 54 to 194 μs at 20 μs intervals. The other imaging parameters were: TR = 2 ms, FOV = 10 cm, a = 3°, 64 pixel resolution, 4096 averages and an 18 min acquisition time.

Quartz fine aggregate (Atlantic Silica, Sussex, NB) and Type 10 Portland cement (Lafarge, Bath, ON) were used to prepare the mortar with a water to cement ratio of 0.5. The mortar was prepared in accordance with ASTM 1260. A cylindrical specimen 43 mm in diameter and 50 mm long was cast and cured under sealed conditions for 3 days at 23 °C. The specimen was oven dried at 105 °C for 2 days prior to exposure to lithium nitrate solution (30%). Teflon tape was applied to the curved surface of the specimen. The specimen was then placed such that the bottom of the cylinder was submerged approximately 1–2 mm into a lithium nitrate solution (Lifetime N, FMC, Bessemer City, NC). The specimen was removed from the solution for imaging. MR and sample mass measurements were performed as a function of time. Measurements were performed after 3, 6, 9, and 22 h of contact with the $LiNO_3$ solution. The imaging parameters were: FOV = 10 cm, $t_p = 30$ μs, TR = 2 ms, $\alpha = 3°$, 64 pixel resolution, $G_{max} = 640\ mTm^{-1}$, 4096 averages in an acquisition time of 18 min.

## Acknowledgments

B.J.B. thanks NSERC of Canada for equipment and operating grants. B.J.B. also thanks the Canada Chairs program for a Research Chair in MRI of Materials (2002–2009). The MRI Center is supported through an NSERC Major Facilities Access award. Special thanks to Rodney P. MacGregor for his help in designing and building the dedicated 1D gradient system.

## References

[1] M.D. Hurlimann, Diffusion and relaxation effects in general stray field NMR experiments, J. Magn. Reson. 148 (2001) 367–378.
[2] P.J. McDonald, Stray field magnetic resonance imaging, Prog. Nucl. Magn. Reson. Spectrosc. 30 (1997) 69–99.
[3] P.M. Glover, P.J. McDonald, B. Newling, Stray-field imaging of planar films using a novel surface coil, J. Magn. Reson. 126 (1997) 207–212.
[4] P.M. Glover, P.S. Aptaker, J.R. Bowler, E. Ciampi, P.J. McDonald, A novel high gradient permanent magnet for profiling of planar films and coatings, J. Magn. Reson. 139 (1999) 90–97.
[5] J. Godward, E. Ciampi, M. Cifelli, P.J. McDonald, Multidimensional imaging using stray-field and pulsed gradients, J. Magn. Reson. 155 (2002) 92–99.
[6] K. Kopinga, L. Pel, One-dimensional scanning of moisture in porous materials with NMR, Rev. Sci. Instr. 65 (1994) 3673–3681.
[7] K. Potter, B.J. Balcom, T.A. Carpenter, L.D. Hall, The gelation of sodium alginate with calcium ions studied by magnetic resonance imaging (MRI), Carbohydr. Res. 257 (1994) 117–126.
[8] B.J. Balcom, R.P. MacGregor, S.D. Beyea, D.P. Green, R.L. Armstrong, T.W. Bremner, Single-point ramped imaging with $T_1$ enhancement (SPRITE), J. Magn. Reson. A 123 (1996) 131–134.
[9] I.V. Mastikhin, H. Mullally, B. MacMillan, B.J. Balcom, Water content profiles with a 1D centric SPRITE acquisition, J. Magn. Reson. 156 (2002) 122–130.
[10] J. Leggett, S. Crozier, R.W. Bowtell, Actively shielded multi-layer gradient coil designs with improved cooling properties, J. Magn. Reson. 165 (2003) 196–207.
[11] R. Bowtell, P. Robyr, Multilayer gradient coil design, J. Magn. Reson. 131 (1998) 286–294.
[12] E.M. Haacke, R.W. Brown, M.R. Thompson, R. Venkatesan, Magnetic Resonance Imaging: Physical Principles and Sequence Design, Wiley, New York, 1999.
[13] R. Freeman, A Handbook of Nuclear Magnetic Resonance, Longman Group, UK, 1998.
[14] C. Brevard, P. Granger, Handbook of High Resolution Multinuclear NMR, Wiley, New York, 1981.
[15] G.R. Ziegler, Oil Migration in Fat-Based Confectionery, 58th Production Conference of PMCA, 2004 April 26–28.
[16] T.M. Guiheneuf, P.J. Couzens, H.J. Wille, L.D. Hall, Visualisation of liquid triacylglycerol migration in chocolate by magnetic resonance imaging, J. Sci. Food Agric. 73 (1997) 265–273.
[17] P. Walter, P. Cornillon, Lipid migration in two-phase chocolate systems investigated by NMR and DSC, Food Res. Int. 35 (2002) 761–767.
[18] P.J. Prado, B.J. Balcom, M. Jama, Single-point magnetic resonance imaging study of water adsorption in pellets of Zeolite 4A, J. Magn. Reson. 137 (1999) 59–66.
[19] R.A. Komoroski, J.M. Pearce, J.E.O. Newton, The distribution of lithium in rat brain and muscle in vivo by Li-7 NMR imaging, Magn. Reson. Med. 38 (1997) 275–278.
[20] M.A. Berube, C. Tremblay, B. Fournier, M.D. Thomas, D.B. Stokes, Influence of lithium-based products proposed for counteracting ASR on the chemistry of pore solution and cement hydrates, Cem. Con. Res. 34 (2004) 1645–1660.
[21] S. Diamond, Unique response of $LiNO_3$ as an alkali silica reaction-preventive admixture, Cem. Con. Res. 29 (1999) 1271–1275.
[22] W.J. McCoy, A.G. Caldwell, New approach to inhibiting alkali-aggregate expansion, J. Am. Con. Inst. 47 (1951) 693–706.